Pol. J. Environ. Stud. Vol. XX, No. X (XXXX), 1-15
DOI: *10.15244/pjoes/214184* ONLINE PUBLICATION DATE: 2026-05-14

Original Research

Strength Monitoring Technology of Loess Slope Based on Distributed In-Situ Monitoring

Zunli Teng°*

College of Civil Engineering, Longdong University, Qingyang, 475000, China

Received: 27 August 2025
Accepted: 12 November 2025

Abstract

Loess soil is widely distributed in northwest China and has a layered structure and developmental characteristics. The stability of multi-level loess slopes under earthquake action has always been a concern, and the shear strength of loess directly affects the strength of loess slopes. Therefore, it is urgent to monitor the shear strength of loess. To achieve precise monitoring of the shear strength of loess, this study proposes a distributed in-situ monitoring method that integrates the active heating fiber method of the moisture field with Bragg grating. This study first analyzes the distributed in-situ monitoring method that combines the active heating fiber method of the water field with Bragg grating, and then constructs a loess slope strength monitoring model based on distributed in-situ monitoring. The testing and analysis results of the proposed model showed that as time increased, the temperature rise of loess with higher moisture content decreased. When the moisture content of loess was 4% and 20%, the maximum temperature rise of loess was 30°C and 20°C, respectively. Overall, the shear strength of loess gradually increased with the increase of dry density. The research model can accurately monitor the resilience of loess slopes, providing reliable technical support for the prediction and early warning of loess slope landslides on reservoir banks.

Keywords: distributed, in-situ monitoring, loess slope, intensity monitoring, active heating, actively heated fiber optic, Bragg grating

Introduction

As one of the common structural forms in various construction projects, the stability of loess slopes has always been a focus of attention in the engineering field [1]. Loess is widely distributed in most regions of China, including Gansu, Shaanxi, and Shanxi, as well as in some areas of Henan, Ningxia, and Hebei. The complex physical and mechanical properties, as well as the ever-changing environmental conditions, make the stability of slopes particularly complex and difficult to predict [2]. With the in-depth implementation of the "Belt and Road" construction policy, infrastructure construction in northwest China is in full swing, and loess slope stability monitoring and assessment are extremely important [3]. Traditional methods for monitoring slope stability often rely on on-site investigations, physical and mechanical tests, and numerical simulations. Although these methods can reflect the stability status of slopes to some extent, they often have problems such as limited monitoring range, poor real-time performance, and a

*e-mail: 18009341102@163.com
°ORCID iD: 0009-0007-0602-8038

low degree of automation [4, 5]. As a consequence of the advancement of scientific and technological knowledge, contemporary slope monitoring technology is evolving in a direction that encompasses automation, remote monitoring, wireless sensing, distribution, and high precision. For example, InSAR technology has been developed into a more conventional monitoring method for small surface deformation, which has the advantages of flexible observation mode, stable equipment, and simple and fast data processing. At present, the application of slope monitoring technology has involved a variety of advanced monitoring means, including "3S" technology, the active heating fiber method, and the Bragg grating sensor. The Actively Heated Fiber Optic (AHFO) method is an effective technique for monitoring moisture migration in unsaturated soils [6]. This method provides real-time monitoring of water migration in unsaturated soil through AHFO sensors, which is of great significance for understanding the mechanisms of geological disasters and environmental geotechnical problems. The AHFO method is not only suitable for research under laboratory conditions but also for on-site monitoring. For example, Ashry et al. could accurately identify and locate the deep sliding surface of landslides by applying distributed fiber optic sensing technology, allowing them to explore the internal deformation laws of landslides. This method has also been applied in the analysis of temperature field characteristics of frozen soil phase transition, providing important technical support for frozen soil engineering. The AHFO method has demonstrated its unique advantages in monitoring the migration of unsaturated soil moisture [7]. Smirnov and Butov analyzed the sources and distribution characteristics of errors in single-probe and double-probe methods through indoor soil column tests, further improving the accuracy and reliability of monitoring [8]. Shadab et al. from the Communication Research Center in Ottawa, Canada, in 1978, first discovered the photosensitivity of germanium-doped quartz fibers and used the standing wave method to fabricate the world's first fiber grating. In the following decade, Fiber Bragg Gratings (FBG) have been one of the research hotspots in fiber optic communication and fiber optic sensing. FBG was an optical device composed of numerous parallel slits of equal width and spacing, usually made by engraving a large number of parallel notches on a glass sheet [9]. The scratch was an opaque part, while the smooth part between the two scratches could be transparent, equivalent to a slit. FBG has a wide range of applications. Presti et al. applied FBG sensors to the field of fiber optic communication and sensing, providing instantaneous and rich sensing information for modern ship operations, ensuring the safety of ships [10]. Rohan et al. mentioned in their latest review on the application of FBG sensors in the biomedical field that FBG sensors have been widely used in various fields such as surgical equipment, vital sign detection equipment, invasive surgery, heart rate, dental applications, and biosensing applications [11]. However, at present, no relevant studies have deeply integrated AHFO and FBG technologies. To achieve accurate monitoring of the shear strength of loess, this study innovatively proposes a monitoring method that utilizes AHFO and FBG technology for distributed in-situ monitoring of loess slope strength. Although the slope monitoring technology proposed by Ashry et al. has a wide spatial coverage and can achieve macroscopic deformation monitoring of large-scale slopes, it is greatly disturbed by factors such as atmospheric delay and surface vegetation coverage, making it difficult to capture the subtle deformation in the shallow layer of the slope. Moreover, it is impossible to directly obtain soil moisture parameters, and the judgment of slope stability needs to be combined with other data. The AHFO module in this research can achieve distributed monitoring of the moisture field, and the FBG module can achieve high-precision capture of strain and displacement parameters. After the integration of the two, water field and stress-strain field data can be obtained simultaneously, directly reflecting the coupling relationship between water migration and the change of slope shear strength. Moreover, the in-situ monitoring method further reduces external interference and has better accuracy and stability.

Methods and Materials

Distributed In-Situ Monitoring Method Integrating AHFO Technology and FBG Sensor

AHFO is a technology used to monitor water migration in unsaturated soils. It uses FBG sensors to monitor the real-time migration of moisture in unsaturated soil, which is developed based on distributed fiber optic temperature measurement technology [12]. The monitoring principle of AHFO technology is shown in Fig. 1.

In Fig. 1, the moisture field active heating fiber method uses the Raman scattering effect to generate forward Stokes light and backward anti-Stokes light by detecting the transmission of light in the fiber [13]. The intensity of anti-Stokes light increases with the increase in temperature, and the temperature value can be deduced by measuring the change in its intensity. Combined with time domain reflectometry, the system can accurately locate the scattering position of light. However, the active heating fiber optic method is usually limited to point or local measurements. Therefore, this study achieves quasi-distributed measurement by placing multiple FBGs on a single optical fiber, monitoring temperature changes at multiple points, and improving monitoring efficiency and range [14]. The principle of FBG sensing is shown in Fig. 2.

In Fig. 2, the working principle of FBG is based on the reflection and interference of gratings [15]. FBG is mainly divided into three layers, namely the core layer, cladding layer, and coating layer. The middle few segments form a grating, with a grating period formed

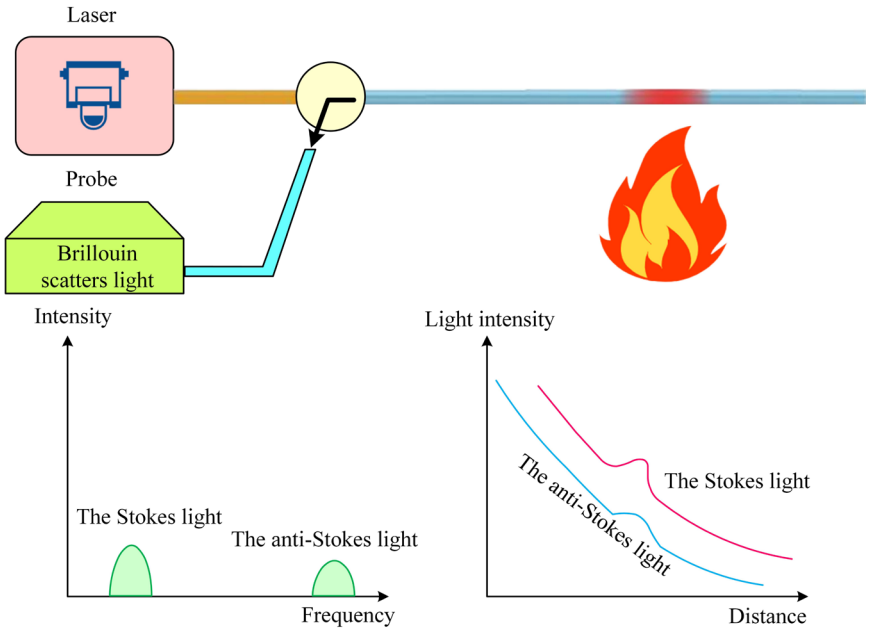

Fig. 1. Actively heated fiber optic method diagram.

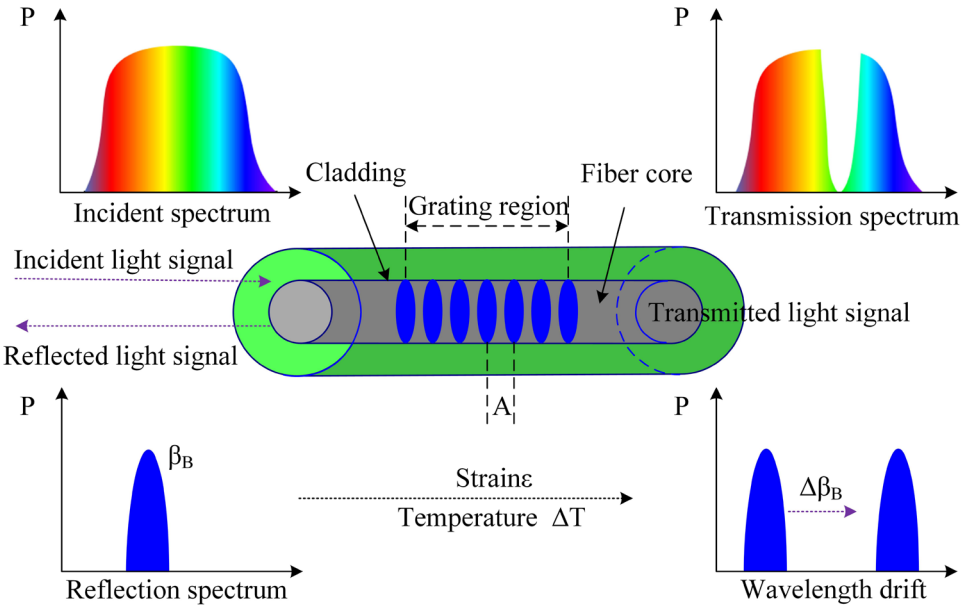

Fig. 2. FBG sensing schematic diagram.

between every two segments. When light waves that meet the Bragg condition encounter these gratings, they will be reflected back and form peaks based on the principle of light superposition. The peak center on the x-axis is recorded as the Center Wavelength (CW) of the FBG. The calculation formula for the CW β_B of the FBG reflection spectrum is shown in Equation (1).

$$\beta_B = 2n_{eff}K \tag{1}$$

In Equation (1), n_{eff} is the effective refractive index of the fiber core. Symbol K is the grating period of the grating region. In the process of using FBG for structural strain measurement, when FBG is subjected to axial stress, the reflection spectrum of FBG will cause a significant drift of the CW [16]. Assuming that the FBG is subjected to uniformly distributed axial strain and stress is uniformly applied along the length direction of the FBG, the expression for the axial stress σ_{ZZ} acting on the FBG is shown in Equation (2).

$$\sigma_{ZZ} = -P_Z, \sigma_{rr} = \sigma_{\theta\theta} = 0 \tag{2}$$

In Equation (2), P_Z is the axial stress. The strain of FBG in each axis can be measured by the Bragg wavelength shift caused by stress-strain. The strain calculation formula for FBG in each axial direction is shown in Equation (3).

$$\rho_{ZZ} = -\frac{P_Z}{E_l}, \rho_{rr} = \rho_{\theta\theta} = -\nu\rho_{ZZ} = \nu\frac{P_Z}{E_l} \tag{3}$$

In Equation (3), E_l is the elastic modulus of FBG. ν is the Poisson's ratio of FBG. FBG is a device that utilizes the periodic refractive index variation of optical fibers to achieve optical waveguides, and the variation of its CW is related to strain and temperature. When FBG is subjected to axial strain, there is a linear relationship between the drift of its CW and the strain. This linear correlation makes it possible to measure changes in external physical quantities, such as strain, temperature, etc., by measuring changes in the CW of FBG. The formula for the CW drift $\Delta\beta_B$ of FBG is shown in Equation (4).

$$\Delta\beta_B = Y_\rho \cdot \rho + Y_T \cdot \Delta T \tag{4}$$

In Equation (4), Y_T is the temperature sensitivity coefficient of FBG. ΔT is the temperature change. The differential grating temperature compensation method is an effective technique for reducing the impact of temperature changes on the measurement results of FBG sensors [17]. This method compensates for wavelength changes caused by temperature through specific structural design and data processing methods, thereby improving the accuracy of sensor measurements [18]. The principle of this method is shown in Fig. 3.

In Fig. 3, when an external force is applied to the sensor, both FBG3 and FBG4 will simultaneously experience the effects of strain and temperature. FBG3 is encapsulated on the tensile strain side of the structure, and the grid spacing of FBG3 will increase accordingly. According to the basic principle of FBG, this will cause the CW of the reflected spectrum to shift towards longer wavelengths, known as the “red shift” phenomenon. FBG4 is situated on the side subjected to compressive strain, and its response is manifested as a reverse compressive strain effect, resulting in a reduction in the distance between fiber optic grids. This, in turn, causes the CW of the reflected spectrum to shift towards shorter wavelengths, a phenomenon known as the “blue shift” [19]. The expression for the CW drift of FBG3 is shown in Equation (5).

$$\Delta\beta_{B3} = Y_\rho\rho Y_{T3}\Delta T + Y_{\rho 3}\rho \tag{5}$$

In Equation (5), $Y_{\rho 3}$ and $Y_{\rho 3}$ are the sensitivity coefficients of strain and temperature for FBG3. The expression between the CW drift of FBG4 and strain and temperature is given by Equation (6).

$$\Delta\beta_{B4} = Y_{T4}\Delta T - Y_{\rho 4}\rho \tag{6}$$

In Equation (6), the sensitivity coefficients of temperature and strain for FBG4 are represented by symbols $Y_{\rho 4}$ and $Y_{\rho 4}$, respectively. When the properties of FBG3 and FBG4 materials are consistent, the strain formula for FBG is given by Equation (7).

$$\rho = \frac{\Delta\beta_{B3} - \Delta\beta_{B4}}{2Y_\rho} \tag{7}$$

The formula for calculating the temperature change experienced by FBG is given by Equation (8).

$$\Delta T = \frac{\Delta\beta_{B3} + \Delta\beta_{B4}}{2Y_\rho} \tag{8}$$

The workflow diagram of AHFO-FBG is shown in Fig. 4.

As can be seen from Fig. 4, the AHFO path emits a laser to the sensing fiber through the excitation source. When a laser is transmitted in optical fibers, Raman scattering occurs. The anti-Stokes light within it is highly sensitive to temperature, and its intensity increases with rising temperature, thus being captured as the core signal. The FBG path modulates the central wavelength of the fiber Bragg grating according to the changes in external physical quantities. The demodulator senses changes in physical quantities by collecting the central wavelength reflected back and its drift amount. The optical signals collected by the two paths are transmitted back through the sensing optical fiber network. The system utilizes time-domain reflectometry technology. By calculating the time it takes for the optical signal to return, it can precisely locate the specific position of the measurement point on the optical fiber, which is the key to achieving distributed and quasi-distributed monitoring. The AHFO demodulator directly calculates the temperature value at each point along the optical fiber by analyzing the light intensity of the anti-Stokes light, forming a distributed temperature field. FBG first measures the drift of the central wavelength. Then, it determines whether a differential grating structure is adopted for temperature compensation. If not used, it calculates the strain or temperature. If differential gratings are used, the wavelength changes of the two gratings are calculated separately to decouple and accurately obtain the strain and temperature change values, and the final results are output.

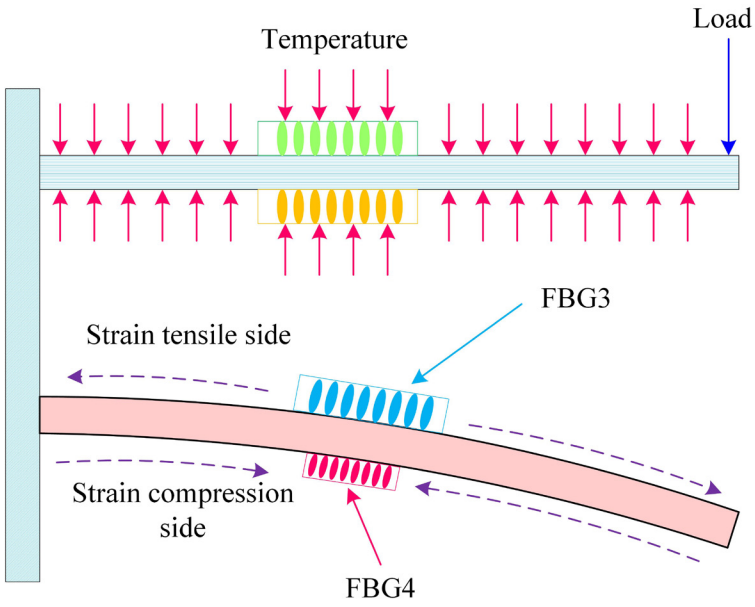

Fig. 3. Differential grating temperature compensation method schematic diagram.

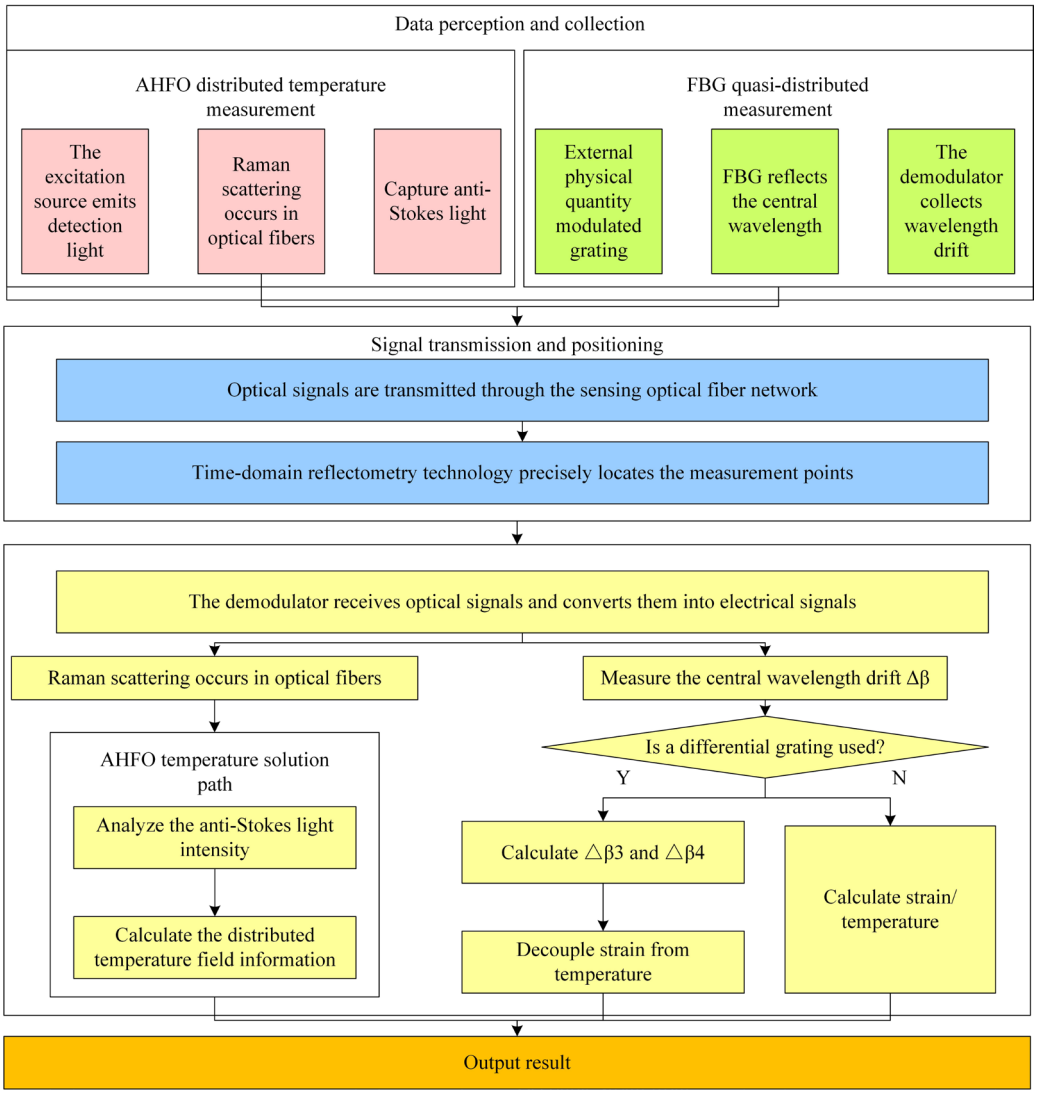

Fig. 4. Workflow diagram of AHFO-FBG.

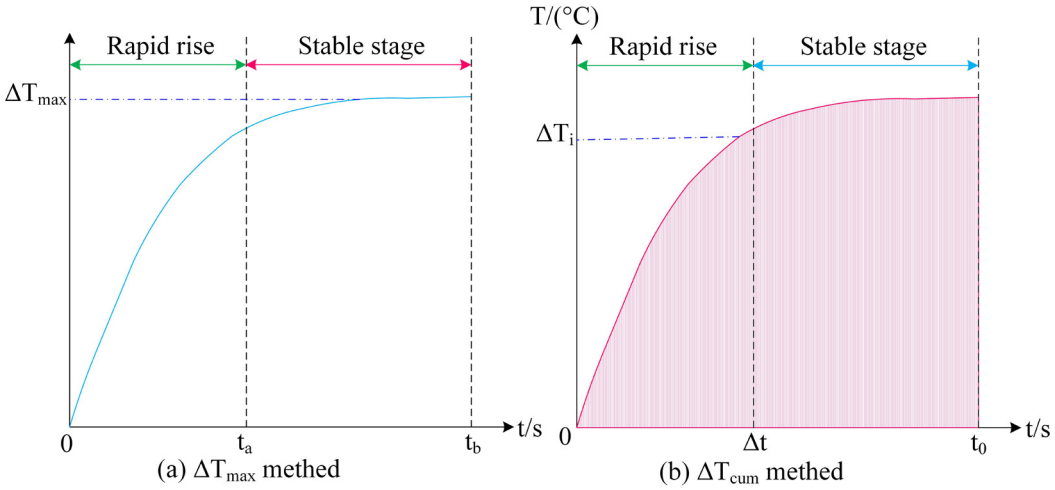

Fig. 5. Schematic diagram of two methods for estimating water content.

Construction of Strength of Loess Slopes Monitoring Model Based on Distributed In-Situ Monitoring

The northwest region is known for its arid climate, with most areas receiving less than 500 millimeters of annual precipitation, belonging to a continental arid, semi-arid, and alpine climate. The annual precipitation on the Loess Plateau is between 300-500 mm, while the precipitation in the Hexi Corridor and Turpan region is even lower, with almost no rain throughout the year. Given such harsh natural conditions, monitoring of loess slopes is imperative. This is the key to ensuring the stable operation of projects like pumped storage power stations in the region. This study integrates AHFO and FBG sensors, combined with online distributed in-situ monitoring of temperature characteristic values, to achieve real-time monitoring of the strength of loess slopes [20]. The expression for the strength of the loess slopes monitoring model that integrates AHFO and FBG sensors is Equation (9).

$$\alpha = \alpha(T_t) \tag{9}$$

In Equation (9), α is the Moisture Content (MC) of loess. T is the temperature characteristic value. The relationship between the strength of the loess slopes parameters and α is given by Equation (10).

$$\begin{cases} c = c(\alpha) \\ \lambda = \lambda(\alpha) \end{cases} \tag{10}$$

In Equation (10), c and λ are the cohesion and the internal friction angle of loess [21]. The expression for the relationship between the c and λ and temperature characteristic values is shown in Equation (11).

$$\begin{cases} c = C(T_t) \\ \lambda = \mu(T_t) \end{cases} \tag{11}$$

The relationship between the strength of loess slopes monitoring and temperature is given by Equation (12).

$$\tau_f = C(T_t) + \varepsilon_f \tan\mu(T_t) \tag{12}$$

In Equation 12, ε is the total normal stress on the failure surface when loess is damaged. In the monitoring process of temperature rise data during the optimization heating stage, the influence of thermal characteristics and contact thermal resistance on the strength of loess slopes evaluation is significant. This is mainly because loess, as a special soil material, has physical and mechanical properties, especially shear strength, which are affected by various factors like temperature and MC [22, 23]. Therefore, this study tests its MC. The testing methods for MC are divided into Temperature Characteristic Value Measurement Algorithm and Cumulative Heating Value Calculation Method [24]. Two methods for calculating MC are shown in Fig. 5.

In Fig. 5, the measurement method of temperature characteristic values is to calculate MC by monitoring the temperature change characteristics of the substance during the heating process. This includes recording parameters such as the time, rate, or temperature difference after heating to a specific temperature, and establishing mathematical models or empirical formulas to invert MC. The calculation method for cumulative temperature rise focuses on the total temperature change during the heating process. It evaluates moisture content by calculating the cumulative temperature rise of the temperature change curve. The expression for the temperature characteristic value ΔT_t is given by Equation (13).

$$\Delta T_t = \frac{\sum_{i=1}^{n} \Delta T_i}{n} \tag{13}$$

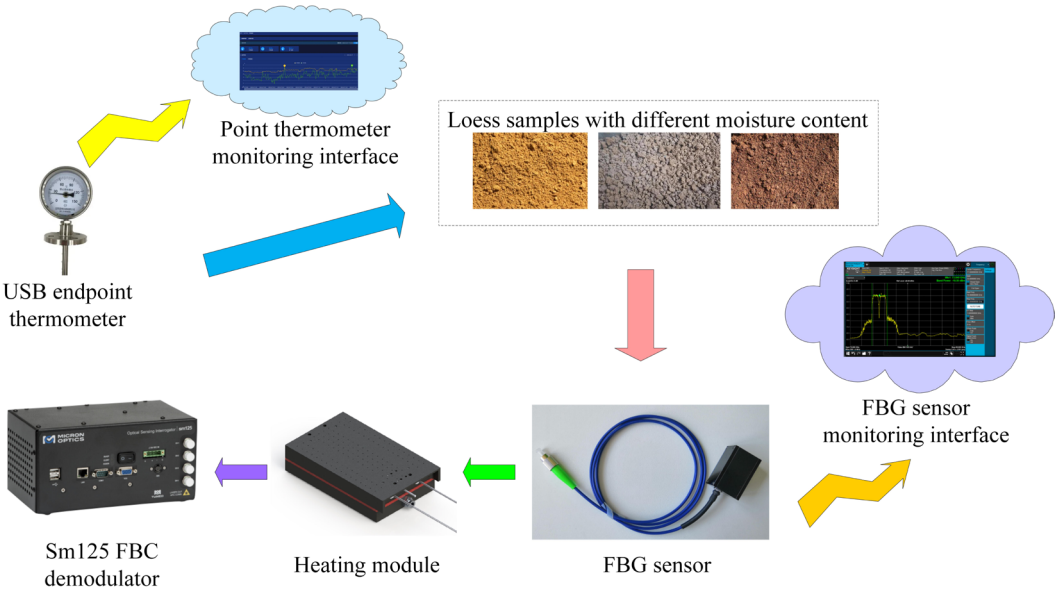

Fig. 6. Water content calibration flow chart of loess based on distributed in-situ monitoring.

In Equation (13), ΔT_i is the temperature change value during a certain period in the stable phase. n is the number of temperature measurements taken during that time period. The expression for the maximum temperature rise value $\Delta T_{\max}$ is given by Equation (14).

$$\Delta T_{\max} = T_{\max} - T_0 \tag{14}$$

In Equation (14), $T_{\max}$ is the maximum temperature value of the corresponding sensor during the heating process. T_0 is the initial sensor temperature value, which is the initial temperature of the soil. The formula for the cumulative heating value ΔT_{cum} is given by Equation (15).

$$\Delta T_{cum} = \int_0^{t_0} \Delta T_m dt \tag{15}$$

In Equation (15), ΔT_m is the temperature change value measured throughout the entire heating process [0, t0]. This study uses the ΔT_{cum} method for calculating MC. The research model uses an exponential function to fit and analyze the shear strength parameters of unsaturated loess with different dry densities. The expression of the exponential function is shown in Equation (16).

$$c = A\exp\left(B\rho_d\right) \tag{16}$$

In Equation (16), $A = 4.61E-3$ and $B = 5.86$. The calibration process diagram of loess MC based on distributed in-situ monitoring is shown in Fig. 6.

In Fig. 6, loess is dried to remove residual moisture, and then finely ground through a 2 mm sieve to screen out impurities. Then, the scientific sampling method is adopted, and the soil samples are sealed and left standing for 48 hours to evenly distribute water [25]. In terms of stress conditions, the research utilized acrylic sheet molds, strictly adhering to the set dry density, to reproduce the historical compaction state of the natural stratum under its own weight through layer-by-layer compaction. Meanwhile, after each layer is compacted, the surface is roughened to weaken the artificial layering surface and enhance the interlayer bonding, thereby more realistically simulating the structure of the on-site soil. To simulate the possible humidity inhomogeneity in the slope and monitor it, a soil trench was specially excavated in the compaction layer in the middle of the mold, and an FBG sensor was embedded. Subsequently, the compaction of the overlying soil layer was continued. This enables the sensor to perceive a soil environment where there may be a humidity gradient vertically, rather than a completely homogeneous sample. After all layers have been compacted, the sample should be left to stand for about 20 min to eliminate the instantaneous rebound after the removal of the compaction equipment and bring the soil sample to a preliminary stable state [26]. The soil samples for the physical index test were taken from the Dongzhi Plateau in the Loess Plateau region. The loess on the Dongzhi Plateau is the standard stratum and classic area for studying loess in China. Its loess sedimentary sequence is complete, and its properties have been deeply and extensively studied in the academic circle. Many classic models and theories regarding the mechanics, hydrology, and engineering characteristics of loess originated from such typical regions. Therefore, the study began sampling 1 m below the top of Dongzhiyuan in 2023, with samples collected every 1 m. To ensure the scientificity and accuracy of the experiment, this study tests the basic physical indicators of loess. To obtain the physical properties of the loess, this study uses methods such as the combined liquid plastic limit tester, oven, and heavy compaction

Table 1. Basic physical index of loess.

Index	Value
Density (g/cm^3)	1.96
Natural MC (%)	24.6
Relative density of soil particles (g/cm^3)	2.71
Liquid limit (%)	26.70
Plastic limit (%)	17.65
Plasticity index (%)	9.05
Optimum MC (%)	12
Maximum dry capacity (%)	1.82

to measure relevant indicators in accordance with the demands of the "Highway Geotechnical Test Code" (JTJ 051-93). Table 1 shows the test results.

To ensure the accuracy of FBG monitoring, this study designs the main structure of FBG based on the requirements of closed pipeline detection, as shown in Fig. 7.

Fig. 7a) shows the installation method of FBG. FBG first ensures that the threaded base is accurately embedded into the predetermined threaded interface of the pipeline. Subsequently, the circular tube is accurately inserted into the circular channel inside the base to achieve preliminary positioning. Then, by rotating the fastening nut and applying appropriate torque along the threaded path on the threaded base, the circular tube body is firmly locked to ensure the structural stability of the entire sensing unit. Fig. 7b) is a schematic diagram of FBG packaging. To address the risk of leakage in fluid dynamics monitoring, this study cleverly embeds sealing rings at the connection interfaces of pipelines, circular pipes, and bases, forming multiple sealing barriers and effectively preventing fluid leakage. Under the said protective measures, the expected service life of the sensor body can reach 15 to 20 years or more, which is in line with the durability of the optical fiber material itself. However, the actual lifespan mainly depends on environmental erosion and mechanical interference. Therefore, an appearance inspection should be conducted every 6 months to 1 year to ensure that the mechanical fasteners are not loose, the casing is not damaged, and there is no excessive bending at the optical cable outlet. Periodically reapply sealant to exposed junction boxes to ensure their waterproof and moisture-proof performance.

Results

Performance Testing of Distributed In-Situ Monitoring Method Integrating AHFO Technology and FBG Sensor

To verify the effectiveness of the distributed in-situ monitoring method that integrates AHFO and FBG, this study selects five types of loess with various initial MCs, namely loess with MCs of 4%, 8%, 12%, 16%, and 20%, for temperature response testing experiments. Fig. 8 shows the experimental results.

Fig. 8 shows the temperature rise monitoring curve of loess with different MCs using the research method. As time increases, the higher the MC of loess, the lower the temperature rise. When the MC of loess is 4% and 20%, the highest temperature rise of loess is 30°C and 20°C. The confidence interval of temperature rise for loess with 4% moisture content is [29.5, 30.5]°C, and that for loess with 20% moisture content is [19.5, 20.5]°C. To verify the influence of heat sources on loess, a research method is used to monitor loess with an MC of 20%. Four temperature monitoring devices are installed in this study at positions 80 mm above the heat source, 40 mm below, and 80 mm below, to accurately record and transmit temperature change data of loess at

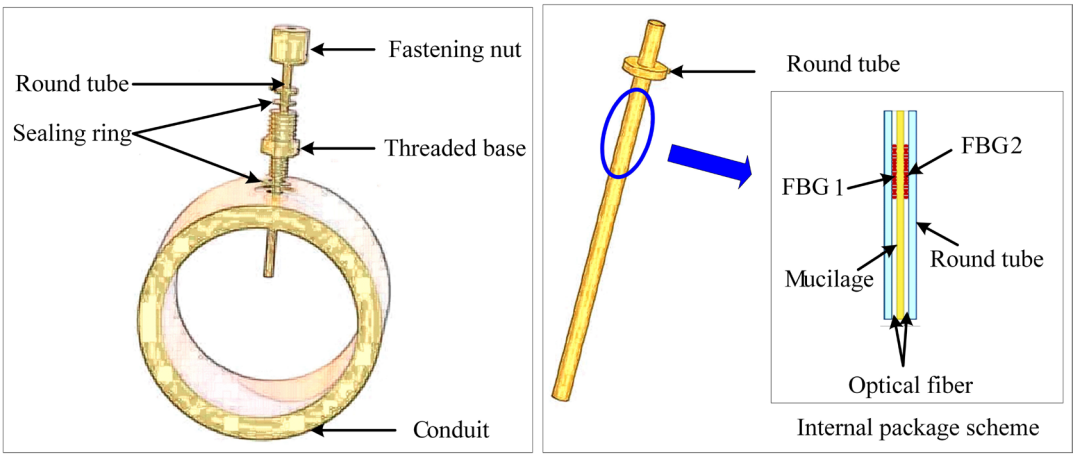

(a)Installation method (b)Package indication

Fig. 7. FBG main structure and package diagram.

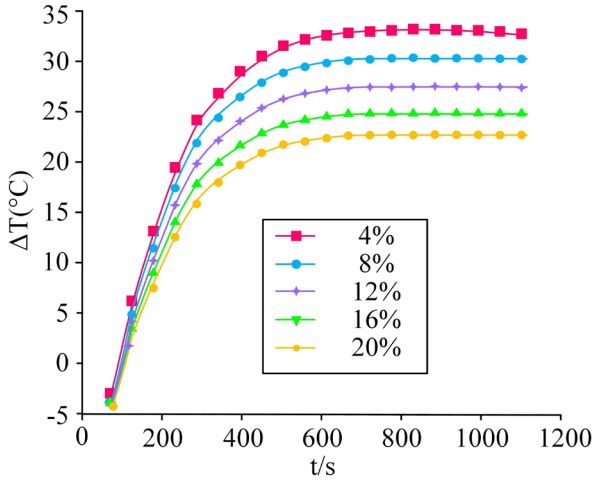

Fig. 8. Temperature rise curve of loess with different moisture content over time.

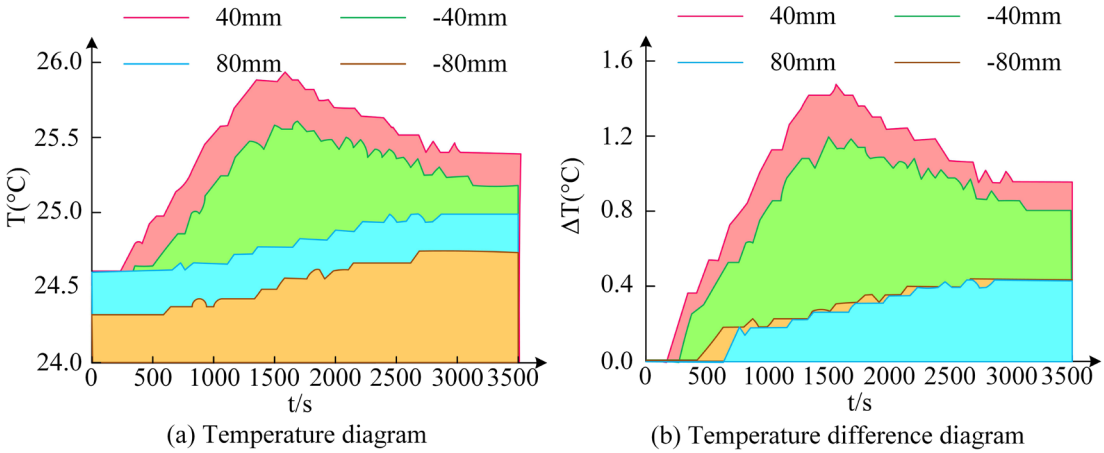

Fig. 9. Temperature curves of loess at different locations.

different distances. The monitoring results are shown in Fig. 9.

Fig. 9a) and b) show the temperature and temperature difference curves of loess at different locations. In Fig. 9a), when the distance from the heat source is 40 mm and -40 mm, and the time is 1500 s, the highest temperatures of the loess are 25.8°C and 25.5°C. At this time, the loess is greatly affected by the heat source. When the distance from the heat source is 80 mm and -80 mm, and the time is 3000 s, the temperature of the loess tends to stabilize. The temperature confidence intervals at 40 mm are [25.3, 26.3]°C, and those at -40 mm are [25.0, 26.0]°C. In Fig. 9b), when the distance from the heat source is 80 mm and -80 mm, the temperature difference is less than 0.4°C within 0-3500 s. This indicates that the heating effect of the heat source on the distant loess is limited, and the temperature of the loess in these locations is less affected by other factors. The confidence interval for temperature difference at 80 mm is [0.3, 0.5]°C, and the confidence interval for temperature difference at -80 mm is [0.2, 0.4]°C. At the same time, it also indicates that the thermal conductivity of loess greatly affects its temperature distribution and changes. In summary, the research results are consistent with the laws obtained from theoretical qualitative analysis, which verifies the rationality of the distributed in-situ monitoring method that integrates active heating fiber and FBG. To explore the relationship between the pore structure and MC of loess, a research method is utilized to monitor the pores and cumulative pore volume of loess with different MCs, as shown in Fig. 10.

Fig. 10a) shows the distribution of porosity components in loess with different MCs. As the MC gradually increases, the proportion of small Pore Size Pores (PSP) shows an increasing trend, while the proportion of medium and large PSPs decreases accordingly. This indicates that the MC has a direct impact on the distribution of pore structure within loess. The confidence intervals for the proportion of small-pore size in loess with 4% moisture content are [30%, 35%],

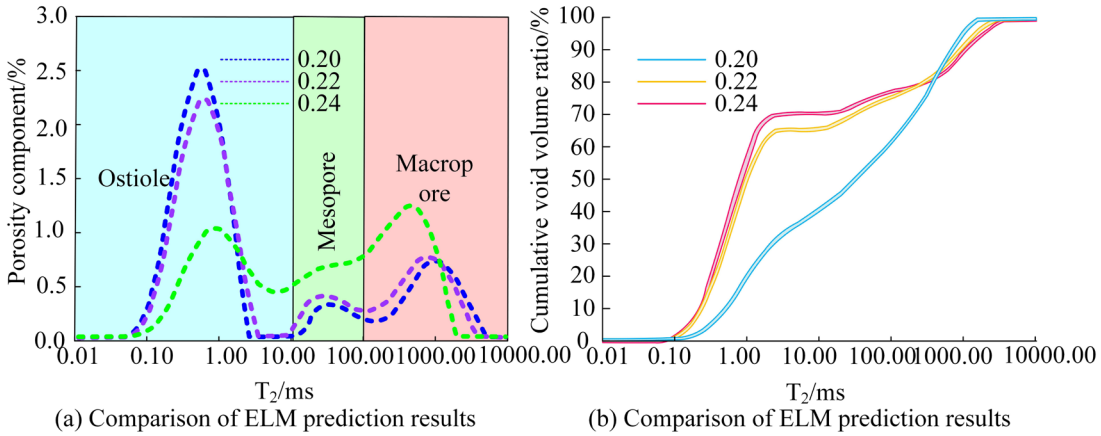

Fig. 10. The results of monitoring loess by the research method.

and those for loess with 20% moisture content are [45%, 50%]. Fig. 10b) shows the distribution of the cumulative pore volume ratio of loess after different MCs. As the MC increases, the cumulative pore volume ratio curve gradually extends towards the low pore size range, and the curve shape tends to become more complex. This is manifested by the alternating appearance of steeper rising segments and more pronounced horizontal segments, indicating an exacerbation of the polarization phenomenon in the distribution of pore sizes in loess. When the MC is 0.20, the cumulative pore volume ratio curve of loess shows the most balanced distribution pattern, with no sharp increase or stable horizontal segment, but rather a uniform distribution of pores within each pore size range. This indicates that loess has the best compaction performance when the MC is 0.20. The stability of loess strength is to some extent influenced by matric suction. The confidence intervals for the cumulative pore volume ratio of loess with 4% moisture content are [20%, 25%], and those for loess with 20% moisture content are [35%, 40%]. The change in Pore Water Pressure (PWP) can, to some extent, reflect the change in matric suction. Therefore, the results of monitoring the PWP of loess at different burial depths using research methods are shown in Fig. 11.

Fig. 11a) and b) show the monitoring results of PWP in loess with 2nd and 3rd grade slope pore pressures. In Fig. 11a), at a burial depth of 1.5 m, the maximum PWP reaches 0.016 MPa, while the minimum value is as low as 0.000 MPa. In Fig. 11b), at the same burial depth of 1.5 m, the maximum PWP increases to 0.022 MPa, while the minimum value decreases to 0 MPa. Therefore, as the burial depth increases, the trend of changes in PWP in loess gradually becomes flat. At a burial depth of 9.5 m, the PWP fluctuates almost stably within a narrow range of 0 MPa to 0.003 MPa. This may be because the sensitivity of deep loess to external environmental factors is significantly reduced, and its PWP state exhibits a high degree of stability.

Analysis of the Strength of Loess Slopes Monitoring Model Results Based on Distributed In-Situ Monitoring

The variation in mechanical properties of loess materials is mainly attributed to changes in MC and dry density. The dry density variation of loess is relatively limited. This study comprehensively evaluates the strength characteristics of loess at different spatial locations through distributed monitoring methods. Firstly, this study sets the MC of loess to the optimal value of 20% to ensure that the experimental results only reflect the impact of changes in dry density. The experiment uses loess samples with the optimal MC and prepares samples with different dry densities, namely 1.5 g/cm³, 1.6 g/cm³, 1.7 g/cm³, and 1.8 g/cm³, through compression techniques. The Stress-Strain Curves (SSC) of unsaturated loess with different dry densities are exhibited in Fig. 12.

Fig. 12(a-d) show the SSCs of loess with dry densities of 1.5 g/cm³, 1.6 g/cm³, 1.7 g/cm³, and 1.8 g/cm³. In Fig. 12a), when the loess pressure is 50 KPa, the shear stress value of the loess is the lowest, at 65 KPa. In Fig. 12b), when the loess pressure is 100 KPa, and the shear displacement of loess is 100, the SSC of loess begins to stabilize. In Fig. 12c), as the shear displacement of loess increases, the SSC of loess only tends to stabilize at a shear displacement of 400 when the loess pressure is 300 KPa. At this point, the shear stress of loess is 90 KPa. In Fig. 12d), under a loess pressure of 100 KPa, the SSC of loess tends to stabilize at a shear displacement of 450. Therefore, the shear strength of loess shows a gradually increasing trend with the increase of its dry density. Subsequently, the curve gradually stabilizes, indicating that the loess has undergone a certain degree of deformation during this stage, and its shear performance tends to stabilize. Table 2 shows the research model monitoring the strength of

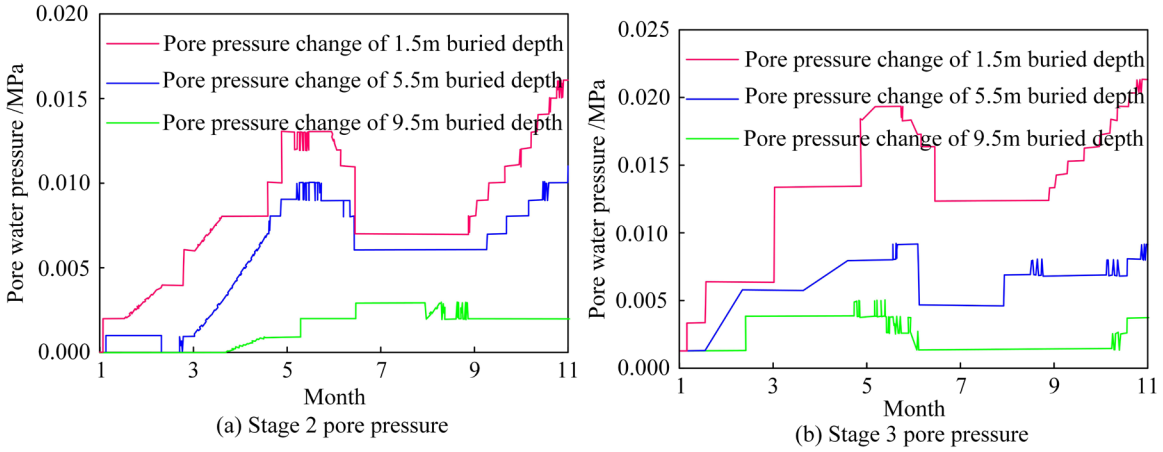

Fig. 11. Monitoring results of PWP in slope.

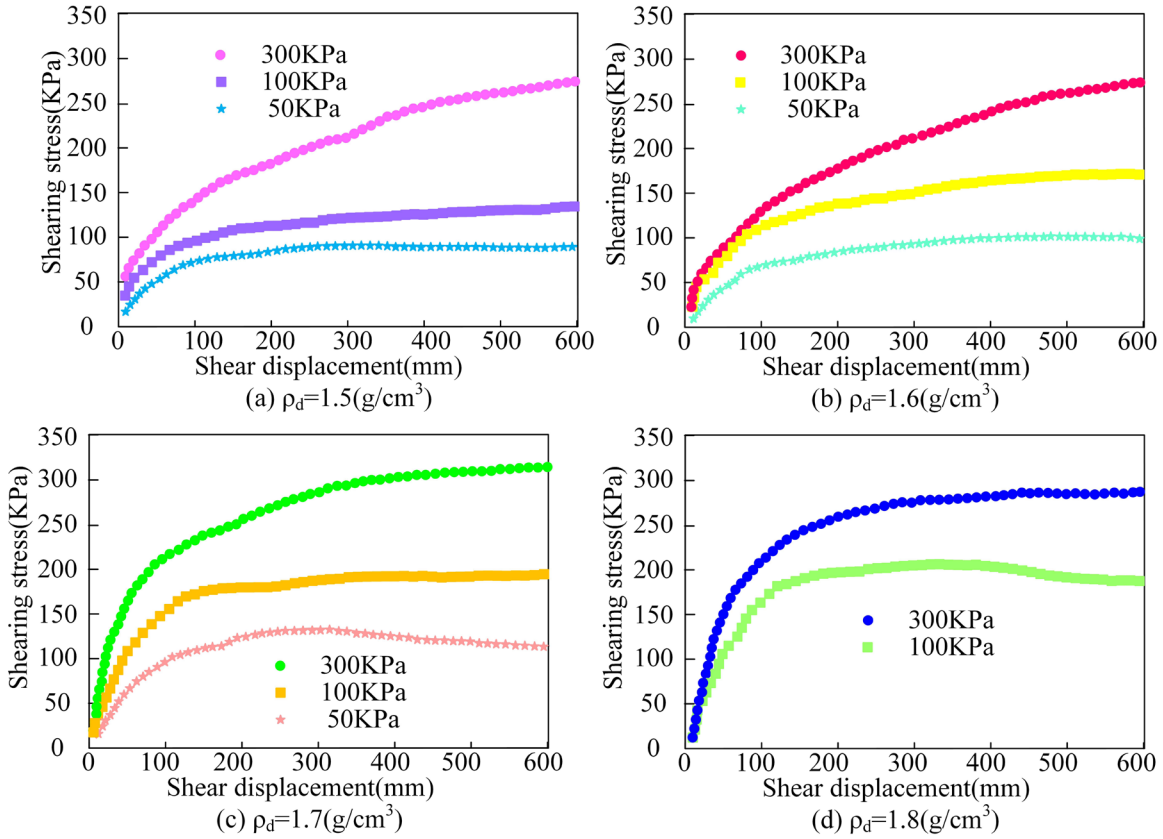

Fig. 12. SSCs of loess with different dry densities.

loess slopes under different dry densities and vertical pressures.

In Table 2, under a vertical pressure of 400 KPa, the strength of loess cannot be tested due to the relatively weak mechanical properties of the 1.5 g/cm³ dry density loess sample. Therefore, in subsequent experiments, this study chooses milder vertical pressure conditions for strength testing, namely 50 KPa, 100 KPa, 200 KPa, and 300 KPa, to ensure the safety of the experimental process and the validity of the data. The research model adopts an exponential function to fit the shear strength parameters of unsaturated loess with different dry densities, and the fitting coefficient R^2 is 0.876. The fitting results are shown in Fig. 13.

Fig. 13a) shows the monitoring map of loess cohesion. As the dry density increases, the cohesion also grows, and the cohesion of loess shows a positive correlation growth trend. The distribution data of cohesion are consistent with the fitting trend of the research model. This indicates the effectiveness and

Table 2. Monitoring results of the loess slope strength under diverse conditions.

Vertical pressure (KPa)	Dry density (g/cm^3)			
	1.5	1.6	1.7	1.8
50	6217	/	/	/
100	86.95	103.19	119.74	/
200	133.46	149.68	170.02	200.00
300	175.82	/	215.73	228.62
400	/	225.06	258.73	266.59

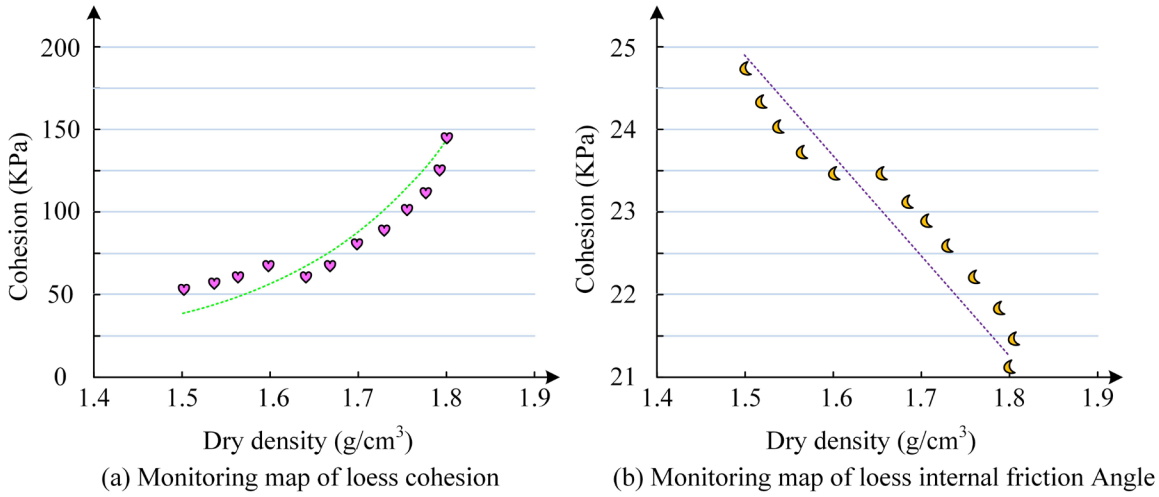

(a) Monitoring map of loess cohesion (b) Monitoring map of loess internal friction Angle

Fig. 13. Shear strength parameters of unsaturated loess with different dry densities.

accuracy of the research model in fitting the complex relationship between cohesion and dry density. Fig. 13b) shows the monitoring map of the internal friction angle in loess. As the dry density increases, the cohesion gradually decreases, and the same research model can fit the cohesion. Therefore, the research model is effective and accurate in fitting the complex relationship between the mechanical properties and dry density of loess. There is usually a positive correlation between cohesion and dry density, while the relationship between internal friction angle and dry density may vary depending on soil type and conditions. The binary fitting diagram of the research model for loess is displayed in Fig. 14.

In Fig. 14, the research model has extremely high accuracy and applicability in predicting the cohesive properties of unsaturated loess, and can achieve binary nonlinear fitting of complex interactions between physical parameters like MC and dry density. This indicates a high degree of consistency between the model's predicted values and the experimental observations, and suggests that the model has strong generalization ability. It can be applied to predict the cohesion of unsaturated loess under different conditions, providing strong theoretical and technical support for geological exploration, slope stability analysis, foundation treatment, and other fields in engineering practice.

Discussion

Loess is a non-layered yellow powdery soil sediment, rich in carbonates, loose, and porous, with vertical joints. This characteristic requires consideration of the special physical properties of loess slopes in their design. Strength of loess slopes analysis involves multiple factors, including soil physical properties, moisture conditions, temperature changes, and external forces. To more accurately and efficiently monitor the state of loess slopes, this study proposes a monitoring technology that integrate active optical fibers and FBG sensors to achieve distributed monitoring of the temperature and mechanical properties of loess slopes.

Firstly, this study analyzed the temperature rise characteristics. The experiments proved that as the MC of loess grew, its temperature rise value showed a downward trend. The sample with the MC of 4% could reach a peak temperature rise of 30°C, while when the MC increased to 20%, the peak temperature rise value dropped to 20°C. This phenomenon indicates the hindering effect of water in the process of heat

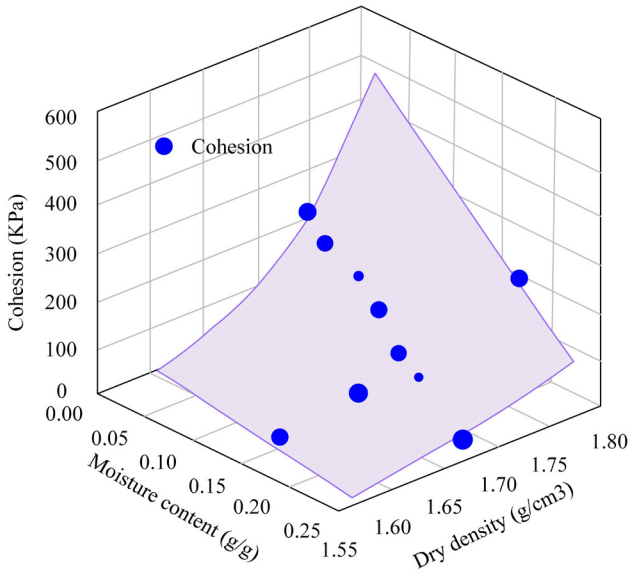

Fig. 14. Schematic of the binary fitting of the study model to loess.

conduction. In addition, research on the relationship between temperature rise and the logarithm of time suggested that when the logarithm of time reached 5, the temperature rise of loess tended to stabilize, indicating the significant characteristics of loess as a thermal resistance medium. This coincides with the research results of Wang et al. on thermal conductivity [27]. Secondly, this study analyzed the temperature distribution and the influence of heat sources, and found that loess located close to the heat source reached a high temperature state in a short period, verifying the significant impact of heat sources on loess in the region. In contrast, at sites situated at greater distances from the heat source, the temperature of the loess exhibited a gradual stabilization over time, accompanied by a relatively minor temperature differential. This outcome validated the precision of the FBG sensor design and lent support to the efficacy of the cylindrical heat source theory. This corresponds with the findings of Guo's team [28]. Then, in the analysis of the pore structure of loess, it was found that the increase in MC led to an increase in the proportion of small PSPs, while the proportion of medium and large PSPs decreased accordingly. This revealed the reshaping mechanism of moisture on the pore structure of loess. The cumulative pore volume ratio distribution map intuitively displayed the polarization phenomenon of pore size distribution. It also pointed out that under a specific MC, the pore distribution of loess reached the optimal equilibrium state, indicating the best compaction effect of loess [29]. This result coincides with Li et al.'s study of the microstructure of compacted loess. Finally, this study analyzed the mechanical properties of loess. The proposed method could accurately fit the positive correlation between loess cohesion and dry density, as well as the trend of internal friction angle changing with dry density, demonstrating the wide applicability and high flexibility of the model [30]. In addition, the method proposed in the research has demonstrated extremely high accuracy and wide applicability in predicting the cohesion characteristics of unsaturated loess. Through the shear strength fitting model, the study can effectively capture the complex interaction between moisture content and dry density, achieving binary nonlinear fitting. The goodness-of-fit R^2 value of this model reached 0.876, indicating that the model has a good fitting effect on the experimental data. The high consistency between its prediction results and the experimental observations verifies the accuracy of the research method. It is consistent with the conclusion of Jia et al. in the study of shear strength of compacted Q3 loess, further consolidating its scientific and practical validity [31].

In summary, the AHFO-FBG technology monitors the temperature, moisture content, and mechanical properties of loess slopes in real time through a distributed sensor network. These data can be transmitted in real time to the central monitoring system, and advanced data analysis algorithms can be used to conduct a real-time assessment of the stability of the slope. Once abnormal changes are detected, the system can immediately issue an alarm to notify relevant personnel to take necessary measures, thereby effectively preventing the occurrence of landslide accidents. The AHFO-FBG technology can also be applied to the early landslide detection infrastructure. By installing sensor networks in potential landslide areas, it is possible to monitor key parameters of loess slopes over the long term [32]. By integrating machine learning and artificial intelligence technologies, in-depth analysis of monitoring data can be conducted to identify early signs of landslides.

Conclusions

This study analyzed the cumulative pore volume distribution of loess with different MCs and found that as the MC gradually increased, the proportion of small PSPs significantly increased, while the proportion of medium and large PSPs decreased accordingly. The morphological changes of the cumulative pore volume ratio curve, especially its extension towards the low pore size range and the complexity of the curve shape, further confirmed the polarization phenomenon of pore size distribution in loess, which intensified with the increase of MC. Based on the in-situ monitoring data of PWP in the slope, it was found that with the growth of burial depth, the trend of PWP in loess tends to flatten out. The research method has demonstrated extremely high accuracy and wide applicability in predicting the cohesive properties of unsaturated loess. This method could effectively capture the complex interaction between MC and dry density, achieving binary nonlinear fitting. The high consistency between its predicted results and experimental observations validated the accuracy of the research method. The distributed in-situ monitoring technology is employed to facilitate the remote distributed monitoring of loess slopes, representing a significant technical advancement in the domain of loess slope monitoring. At the same time, the deformation and strength characteristics of unsaturated undisturbed and remolded loess in Dongzhi Yuan of the Loess Plateau are studied by triaxial shear test, which provides a reference for practical engineering. However, this study also has certain limitations, such as insufficient long-term monitoring data on the changes in the strength of loess slopes under extreme climate conditions, and further strengthening of the model's adaptability verification in complex geological environments. Future research can verify and improve the model by conducting long-term monitoring projects in different climate regions and geological conditions to collect more data. At the same time, by integrating advanced numerical simulation techniques and machine learning algorithms, the predictive ability and adaptability of the model can be further enhanced.

Conflict of Interest

The author claims no conflict of interest.

Fundings

The research is supported by: Technology plan project for Qingyang, Experimental Study on the Evolution Mechanism of Gully Head Erosion Morphology and Experimental Study on Anti-erosion Engineering Measures for Dongzhiyuan, (NO.: QY-STK-2023A-031); Technology plan project for Qingyang, The Research on Construction Quality Control and Safety Risk Supervision for High-Fill Engineering in the Dongzhiyuan's Gully Consolidation and Plateau Protection Project, (No.: QY-STK-2022B-119).

References

1. CHENG Y., HUO A., ZHAO Z., PENG J. Analysis of loess fracture on slope stability based on centrifugal model tests. Bulletin of Engineering Geology and the Environment. **80** (5), 3647, **2021**.
2. SUN X., HO C.H., LI C., XIA Y., ZHANG Q. Inclination effect of coal mine strata on the stability of loess land slope under the condition of underground mining. Natural Hazards. **104** (9), 833, **2020**.
3. ZHUANG J., PENG J., ZHU Y. Study of the effects of clay content on loess slope failure mode and loess strength. Bulletin of Engineering Geology and the Environment. **80** (3), 1999, **2020**.
4. SUN X., MIAO L., WANG H., CHEN R., WU L. Bio-cementation for the mitigation of surface erosion in loess slopes based on simulation experiment. Journal of Soils and Sediments. **22** (6), 1804, **2022**.
5. XIE W., GUO Q., WU J.Y., LI P., YANG H., ZHANG M. Analysis of loess landslide mechanism and numerical simulation stabilization on the loess plateau in central China. Natural Hazards. **106** (7), 805, **2021**.
6. XU Q., LIU F., GAO Z., ZHANG B., TAO X., HE J. Actively Q-switched and mode-locked all-fiber lasers with an α-$BaTeMo_2O_9$-based acousto-optical modulator. Applied Optics. **60** (35), 10838, **2021**.
7. ASHRY I., MAO Y., WANG B., HVEDING F., BUKHAMSIN A.Y., NG T.K., OOI B.S. A review of distributed fiber–optic sensing in the oil and gas industry. Journal of Lightwave Technology. **40** (5), 1407, **2022**.
8. SMIRNOV M., BUTOV O.V. Pump and thermal impact on heavily erbium-doped fiber laser generation. Optics Letters. **46** (1), 86, **2021**.
9. SHADAB A., RAGHUWANSHI S.K., KUMAR S. Advances in micro-fabricated fiber Bragg grating for detection of physical, chemical, and biological parameters--A review. IEEE Sensors Journal. **22** (16), 15650, **2022**.
10. PRESTI D.L., MASSARONI C., LEITAO C.S.J., DOMINGUES M.D.F., SYPABEKOVA M., BARRERA D., FLORIS L., MASSARI L., ODDO C.M., SALES S., IORDACHITA I.I., TOSI D., SCHENA E. Fiber bragg gratings for medical applications and future challenges: A review. IEEE Access. **8** (4), 156863, **2020**.
11. ROHAN R., VENKADESHWARAN K., RANJAN P. Recent advancements of fiber bragg grating sensors in biomedical application: A review. Journal of Optics. **53** (1), 282, **2023**.
12. LIN P., WANG T., MA W., YANG Q., LIU Z. Transmission characteristics of 1.55 and 2.04 μm laser carriers in a simulated smoke channel based on an actively mode-locked fiber laser. Optics Express. **28** (26), 39216, **2020**.
13. YAN W., DONG C., XIANG Y., JIANG S., LEBER A., LOKE G., XU W., HOU C., ZHOU S., CHEN M., HU R., SHUM P.P., WEI L., JIA X., SORIN F., TAO X., TAO G. Thermally drawn advanced functional fibers: New frontier of flexible electronics. Materials Today. **5** (2), 168, **2020**.
14. LI T., GUO J., TAN Y., ZHOU Z. Recent advances and tendency in fiber Bragg grating-based vibration sensor: A review. IEEE Sensors Journal. **20** (20), 12074, **2020**.

15. MISHRA M., SAHU P.K. Fiber Bragg gratings in healthcare applications: A review. IETE Technical Review. **40** (2), 202, **2022**.
16. LOBRY M., FASSEAUX H., LOYEZ M., CHAH K., GOORMAGHTIGH E., WATTIEZ R., CHIAVAIOLI F., CAUCHETEUR C. Plasmonic fiber grating biosensors demodulated through spectral envelopes intersection. Journal of Lightwave Technology. **39** (22), 7288, **2021**.
17. ESPOSITO F., SRIVASTAVA A., SANSONE L., GIORDANO M., CAMPOPIANO S., IADICICCO A. Label-free biosensors based on long period fiber gratings: A review. IEEE Sensors Journal. **21** (11), 12692, **2020**.
18. LAN F., WANG D.N. Long-period fiber grating based on inner microholes in optical fiber. Optics Letters. **47** (1), 146, **2021**.
19. DENG J., CHURKIN D.V., XU Z., SHU X. Random fiber laser based on a partial-reflection random fiber grating for high temperature sensing. Optics Letters. **46** (5), 957, **2021**.
20. MOKAYED H., QUAN T.Z., ALKHALED L., SIVAKUMAR V. Real-time human detection and counting system using deep learning computer vision techniques. Artificial Intelligence and Applications. **1** (4), 221, **2022**.
21. LIU Y., HU X., YU D., ZHU H., LI G. Influence of the roots of mixed-planting species on the shear strength of saline loess soil. Journal of Mountain Science. **18** (3), 806, **2021**.
22. DUAN Z., YAN X., SUN Q., TAN X., DONG C. Effects of water content and salt content on electrical resistivity of loess. Environmental Earth Sciences. **80** (2), 1, **2021**.
23. YANG W., PAN B., JIN L., WANG Y., SALEEM F. Experimental study on dynamic characteristics of Qingyang loess under different water contents. Arabian Journal of Geosciences. **13** (8), 1, **2020**.
24. WANG T., SU L. Experimental study on moisture migration in unsaturated loess under effect of temperature. Journal of Cold Regions Engineering. **24** (3), 77, **2010**.
25. HU W., CHENG W.C., WEN S. Investigating the effect of degree of compaction, initial water content, and electric field intensity on electrokinetic remediation of an artificially Cu-and Pb-contaminated loess. Acta Geotechnica. **18** (2), 937, **2022**.
26. ZHAO F., WU Y., HUI J., SIVAKUMAR B., MENG X., LIU S. Projected soil organic carbon loss in response to climate warming and soil water content in a loess watershed. Carbon Balance and Management. **16**, 1, **2021**.
27. WANG J., DENG J., ZHENG J., WANG T., YU Y. Thermal conductivity of loess: Experimental studies and empirical model. KSCE Journal of Civil Engineering. **28** (2), 644, **2024**.
28. GUO Y., CHEN M., XIONG L., ZHOU X., LI C. Fiber Bragg grating based acceleration sensors: A review. Sensor Review. **41** (1), 101, **2021**.
29. LI P., PAN Z., XIAO T., WANG J. Effects of molding water content and compaction degree on the microstructure and permeability of compacted loess. Acta Geotechnica. **18** (2), 921, **2022**.
30. YUNITA F. T., SOEKARNO I., NUGROHO J., SANTOSA U. B. Empirical model of unconsolidated tephra erosion: verification and application on micro catchment. Civil Engineering Journal. **10** (7), 2088, **2024**.
31. LI J.W., HUI F.H., YE S.X., JUAN Y.X. Characteristics of shear strength and deformation of compacted Q3 loess. Soil Mechanics and Foundation Engineering. **57**, 65, **2020**.
32. NURZAMAN L., JUWONO P.T., DERMAWAN V., WIJATMIKO I. The effectiveness of inclined pile breakwater on the transmission coefficient. Civil Engineering Journal. **10** (6), **2024**.